PAPER • OPEN ACCESS

CFD analysis of a multi-rotor flying robot for air pollution inspection

To cite this article: G Suchanek and R Filipek 2022 *J. Phys.: Conf. Ser.* **2367** 012010

View the article online for updates and enhancements.

CFD analysis of a multi-rotor flying robot for air pollution inspection

G Suchanek[1] **and R Filipek**[1]

[1]AGH University of Science and Technology, Department of Power Systems and
Environmental Protection Facilities, Faculty of Mechanical Engineering and Robotics,
30 Mickiewicza Av., 30-059 Krakow, Poland

E-mail: suchanek@agh.edu.pl

Abstract.   The aim of the work was to create a CFD model of the flow generated around the
drone to estimate the impact of field parameters on the results of actual measurements from
PM sensors that are positioned differently in relation to the propellers. The model created with
the use of the ANSYS Fluent software allowed one to determine the criterion of their sufficient
distance. The robots with four, six and eight rotors were analyzed. For these, the turbulence
intensity, velocity and pressure distributions were determined. The paper also presents the
results of PM measurements carried out under field conditions using two sensors mounted on
the hexacopter robot.

1. Introduction
The polluted air, in particular the high concentration of airborne particles, is one of the main
environmental threats to human health. It is responsible for, i.e., cancer of the respiratory
system, the prevalence of allergies and increases the relative risk of premature death [1]. There
are also less obvious costs, such as environmental costs for, e.g., decaying building facades.
Sources of this type of pollution are, but are not limited to: wildfires [2], low chimney emissions,
heat power plants [3], or other processes where low-quality solid fuels or waste are incinerated.
Therefore, there is a constant need to look for and develop solutions that would make it possible
to locate the sources of this type of pollution. A dedicated multirotor flying robot equipped
with a particle concentration measurement system can be used to autonomously locate sources
of air pollution. However, a robot of this type significantly disturbs the ambient flow of gases
and particulate matter.

The use of multi-rotor robots to measure particulate matter (PM) has been described, among
others, in [4], where measurements were carried out in the city during periods of heavy traffic
with the use of a quadcopter robot and a simple low-cost recorder with particulate matter
sensors. Another example should be mentioned [5], where a mobile robot cart with a low-cost
sensor was developed to map spatial PM distributions over time. However, the use of a wheeled
robot is a great simplification and limitation. In [6], the possibilities of using the low-cost sensor
system were analyzed to obtain reliable data. The paper [7] presents an innovative approach,
where the novelty lies in the fact that the robot can mitigate (only NO_2 for now) the detected
air pollution. Moreover, the effectiveness of this solution is limited by the loading capacity of
the robot. The influence of rotors on the reliability of the measurement was also investigated
[8]. However, no actual units were presented to measure air pollutants. In the work [9], similar
experiments were carried out in both the wind tunnel and the open air, using a quadcopter

robot, an array of low-cost sensors and research-grade instruments. The results have shown that a concentration of $PM2.5$ increases by as much as 400% when comparing the measurements taken before and after the propellers were turned on. The subject of the investigation is also the influence of meteorological factors such as wind and precipitation [10] on the change in PM concentration. Another example may be [11] where low-cost sensors have been evaluated at high altitudes in mountains, where there is lower atmospheric pressure. However, in these there is no answer to the question of how a local change in the ambient conditions caused by the robot affects the measured particles.

On the basis of the above-mentioned examples, it is possible to indicate some research gaps related, but not limited to: analyzing only one robot configuration or the arbitrarily selected location of the measuring system. Therefore, the purpose of the work was to estimate the magnitude of aerodynamic phenomena on an example of robots with four, six and eight rotors. To achieve this goal, it was necessary to determine velocity, turbulence and pressure distributions for a single, two (one above the other), four and six rotor configurations. These distributions were obtained with Ansys Fluent software, widely used to solve academic problems. Finally, particle matter measurements were performed under field conditions to verify whether the results obtained can be explained on the basis of the prepared numeric model.

2. Computational models

As mentioned earlier, the subjects of the analysis were configurations with one, two, four and ultimately six rotors. For these, the velocity, pressure field distributions and turbulent intensity were determined. These configurations are the result of the three analyzed multirotor type quad, hexa, and octocopter robots.
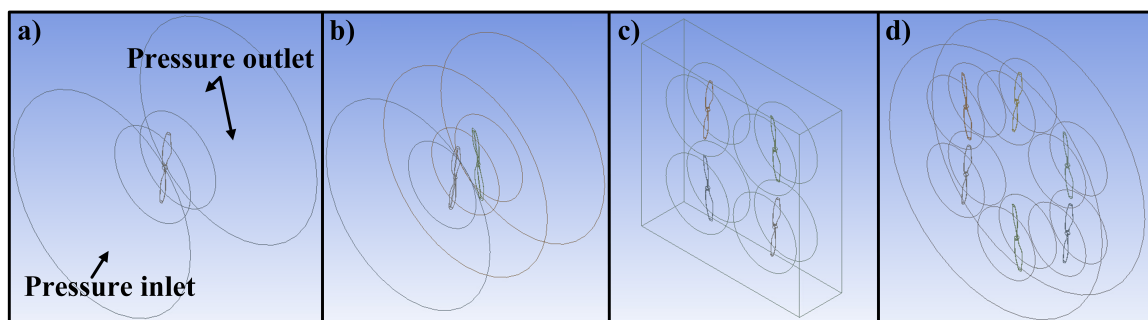

Figure 1. Computational domains: one (a), two (b), four (c), six (d) rotors configurations.

First, a single-rotor reference analysis was performed in a large zone (Figure 1a). Two propellers used in the described robots were analyzed: a smaller 1045 type (diameter of 10 inches and 4.5 inch pitch) and a larger of type 1238 (diameter of 12 inches and 3.8 inch pitch). These conditions corresponded to the conditions during the tests on a dynamometer station. The computational domain for these cases has the shape of a cylinder with dimensions: for a 1045 propeller with a diameter of 0.7 m and height of 0.5 m, for larger one with a diameter of 0.8 m and height 0.6 m. The geometric model of the rotors (propellers) was made in CATIA engineering software based on 3D scans. With various types of propellers with dimensions previously given, it was chosen to scan those that generated the largest thrust, as measured at the dynamometer station. Similarly, on the basis of the measurements, it was possible to determine the rotation of the propeller of the robot in the hover state, which amounted to: 4029 rpm (quad), 4598 rpm (hexa) and 4185 rpm (octo), and such a value was also adopted for simulations.

The first robot analyzed is an octocopter-type robot. It is in a redundant configuration, which means that it has four arms and for each arm there are two drive sets, a top and a bottom one. The total weight of this robot is 4.3 kg and is equipped with a 1238 propeller. Due to the large external dimensions and the high computing complexity that ensues, it was decided to perform

the analysis for a counter-rotating configuration of the two propellers, as shown in Figure 1 b. For this purpose, it was necessary to create two dynamic zones over ourselves, similar to the shape of a cylinder with a diameter of 0.36 m and a height of 0.12 m. Dynamic zones rotate at identical rotational speeds but in opposite directions. The surrounding is the static zone, which is cylinder-shaped with a diameter of 0.8 m and height 0.6 m. The next robot analyzed is a quadcopter robot equipped with four rotors, one on each arm. This robot is equipped with 1045 propellers and weighs 1.35 kg. The prepared geometric model (Figure 1c) includes four cylinder-shaped rotary zones with a diameter of 0.3 m and a height of 0.1 m. The robot environment is a rectangular static zone with dimensions of 0.75 m × 0.75 m × 0.2 m. The construction of a hexacopter robot (Figure 1d) is very similar. It is equipped with the same type of propeller, so the same dynamic zones have been adopted. Additional rotors were taken into account, and in this case the static zone has the shape of a cylinder with a diameter of 0.5 m and a height of 0.2 m. The robot weighs 2.54 kg. In the cases where the configuration of four or six rotors was modeled, the prepared model included only the closest robot environment. This is because the measuring system arm cannot be too far from the center of gravity of the robot because it would severely degrade the stability of the robot in the air.

The next stage of the work was to build computational models in ANSYS Fluent [12]. This fluid flow modeling software solves partial differential equations resulting from the conservation of mass and momentum. Additional transport equations must be added if the flow is turbulent. The mass conservation equation is written in a generalized form as follows

$$\frac{\partial \rho}{\partial t} + \nabla \cdot (\rho \vec{v}) = S_m \tag{1}$$

where ρ is the density of the fluid, $\vec{v}$ is the velocity, and S_m is the mass source. The principle of momentum conservation for an inertial reference frame is described [13] by

$$\frac{\partial}{\partial t} (\rho \vec{v}) + \nabla \cdot (\rho \vec{v} \vec{v}) = -\nabla p + \nabla \cdot (\bar{\bar{\tau}}) + \rho \vec{g} + \vec{F} \tag{2}$$

where p is the static pressure, $\bar{\bar{\tau}}$ is the stress tensor, as well as $\rho \vec{g}$ and $\vec{F}$ are the gravitational body force and external body forces, respectively. The stress tensor $\bar{\bar{\tau}}$ is given by

$$\bar{\bar{\tau}} = \mu \left[\left(\nabla \vec{v} + \nabla \vec{v}^T \right) - \frac{2}{3} \nabla \cdot \vec{v} I \right] \tag{3}$$

where μ is the molecular viscosity, I is the unit tensor, and the second term on the right-hand side is the effect of volume dilation. A direct numerical solution to these equations is known as the DNS (Direct Navier-Stokes) method, but it is impractical due to the very high demand for computing power. In practice, as in these studies, other methods, such as the Reynolds-averaged Navier-Stokes (RANS) method, are widely used. In Reynolds averaging, the solution variables in the instantaneous (exact) Navier–Stokes equations are decomposed into the mean (spatial–averaged or time–averaged) and fluctuating components. For velocity, pressure and other scalar quantity components it is written as

$$u_i = \bar{u}_i + u'_i, \quad \phi = \bar{\phi} + \phi' \tag{4}$$

where $\bar{u}_i$ and u'_i are the mean and fluctuating velocity components $(i = 1, 2, 3)$ as well as $\bar{\phi}$ and ϕ' denote analogously scalar parameters such as pressure, energy or species concentration. The boundary conditions in the model were assumed as shown in Figure 1a, i.e. the upper surfaces of the static zones as the pressure-inlet and the lower and side surfaces as the pressure-outlet. Both the inflow and outflow conditions are based on the known pressure value at the boundary. On these surfaces, the pressure value was assumed to be zero with the reference value of 1 atm. For the modeling of turbulence, a standard $k - \omega$ SST model [14] was used and all calculations were performed for steady state.

For the different rotor configurations analyzed, it was necessary to use the multiple reference frame (MRF) approach. The MRF model is a steady-state approximation. In that approach,

specific rotational speeds are assigned to each rotational zone and the flow in each of them is solved using the equations of the moving coordinate system. A local coordinate system transformation is performed on the internal contact surfaces of the domains (interfaces) between the moving and stationary zones. This allows the flow parameters in one zone to affect the flows at the boundary of an adjacent one. This MRF approach is very computationally efficient, but it is planned to use the sliding mesh (SM) approach [15] in future work, as it is highly accurate for high rotational speeds. In the SM approach, the rotary domain mesh slide relative to the stationary one along the interface surface.

The finite volume method (FVM) based on a nonstructural mesh was used because of the high complexity of the propeller geometry. For example, for the smaller of the propellers, it was defined that the element size in the rotary zone does not exceed 0.003 m, and in a static zone 0.01 m. Furthermore, to consider the aerodynamic phenomena modeled near the rotor as correct, it is necessary to ensure that the dimensionless wall distance y^+ on the entire rotor surface is less than 1. To obtain an y^+ at a specified level, a boundary layer was modeled. This goal was achieved through a significant local refinement of the mesh (figure 2c) on the surface of the wall (rotor). For this purpose, the following parameters were specified: the first layer height of 0.006 mm, 8 boundary layers and 1.2 inflation ratio. The assumed values were the result of a compromise between the required computing power and the accuracy and usability of the model. Further refinement of the mesh did not significantly improve the solution. Figure 2a shows the determined parameters of the force and torque of the rotor, while figure 2b shows the maximum values of the flow velocity in the sections analyzed marked as A, B and C. These sections are located 0.05 m, 0.1 m, and 0.2 m, respectively, below the surface of the rotor. All of these parameters were plotted as functions of a different number of elements. The criterion adopted here is that for the next step in computational mesh refinement, their difference from the previous step changes by less than 10%. In the final case, the difference in the rotor parameters was about 1% and in the case of the speed about 8%. This allowed us to conclude that the grid independence of the solution was obtained.
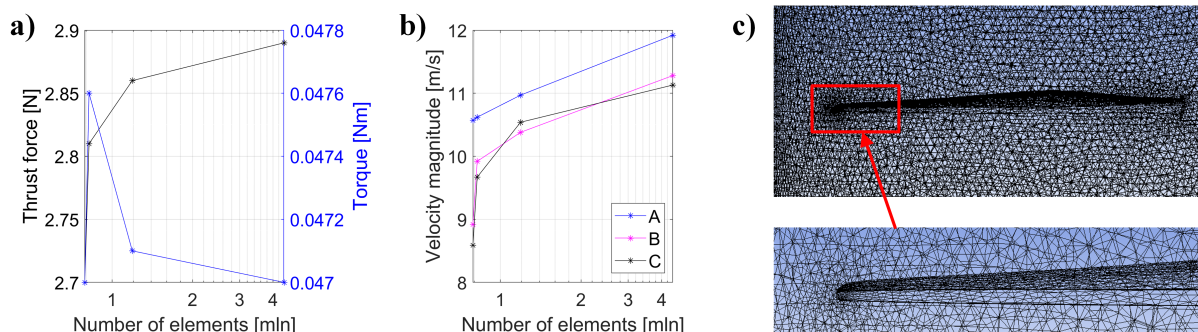

Figure 2. Parameters determined during the examination of the independence of the solution from the computational mesh: a) thrust force and torque, b) velocities, c) mesh — close-up on the rotor surface.

3. CFD simulation results

Figure 3 shows longitudinal sections of the velocity field, axes, as well as A, B, and C marking the cross sections for a single 12 inch wide propeller, which are located 0.05 m, 0.1 m and 0.2 m below the rotor, respectively. In the case of a configuration of two rotors above each other, these distances were defined below the bottom rotor. For these sections, data from the ANSYS Fluent program were collected and then, on this basis, the envelopes of the velocity distribution and turbulent intensity were determined using scripts prepared in Matlab software.

The turbulence intensity parameter is by definition expressed as a percentage and is given as the quotient of the RMS value of the turbulent velocity fluctuations and the mean velocity of
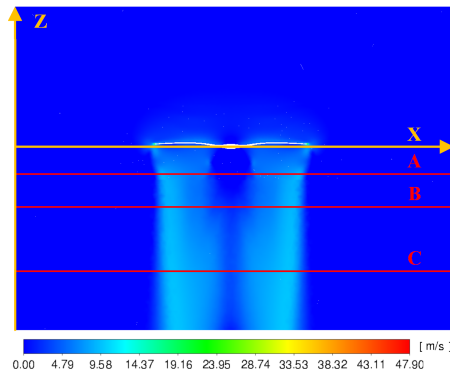
Figure 3. Distribution of the flow velocity magnitude in the cross-section for a single (S) 12-inch rotor with marked perpendicular measurement cross-sections (A,B,C).
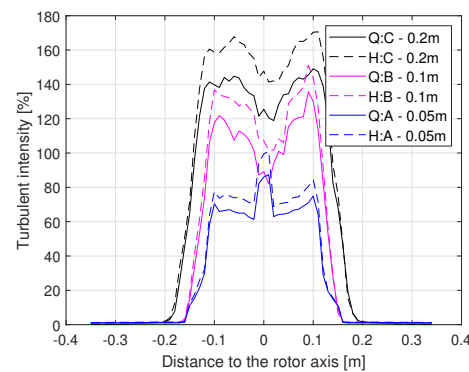

Figure 4. Turbulent intensity in selected cross-sections for the single rotor at rotational speed corresponding to four (Q) and six (H) rotors robots in the hover state.

the flow at the specified point. This value allowed us to compare different configurations and, on its basis, to determine how far the input of the measuring system should be located. Initially, a suitable place was considered, where the intensity level was less than 2 %. Table 1 lists the minimum distances to the rotor axis d_{min} and the flow velocities for those $v(d_{min})$ for which the intensity is lower than the adopted threshold. Values *10 inch Q* and *10 inch H* were determined from 10 inch single propeller models for the operating conditions of: Q - quad-, H - hexacopter. The values *12 inch S* and *12 inch D* denote the 12 inch single (S) and dual (D) propeller configurations for the operating conditions of the octocopter, respectively. From the table 1 it

Table 1. Parameters at analyzed sections for turbulent intensity $< 2\%$.

Section	Parameter	10 inch Q	10 inch H	12 inch S	12 inch D
A	d_{min} $[m]$	0.150	0.150	0.175	0.177
	$v(d_{min})$ $[\frac{m}{s}]$	0.80	0.91	0.80	0.62
B	d_{min} $[m]$	0.153	0.153	0.144	0.174
	$v(d_{min})$ $[\frac{m}{s}]$	0.49	0.55	0.64	0.50
C	d_{min} $[m]$	0.189	0.192	0.175	0.227
	$v(d_{min})$ $[\frac{m}{s}]$	0.27	0.32	0.36	0.32

can be seen that the minimum distance d_{min} is increasing for a configuration with more rotors. It should be noted that this distance is always greater than the radii of the propellers, which are 0.127 m and 0.15 m, respectively. Similarly, the flow speed increases, but for the 2 % threshold adopted it never exceed 1 $\frac{m}{s}$ in all cases. Regarding the distances d_{min}, the differences between sections A and B are small for each configuration. This is due to the fact that for cross section A (which roughly corresponds to the position of the robot arm), the intensity increases rapidly to the level of 10 %, which can be seen in Figure 4. When comparing the configurations of the octocopter robot, it should also be taken into account that the distances for a dual configuration are defined below the bottom rotor, which are 0.11 m, 0.16 m and 0.26 m, respectively, under the axis of the robot arm. In Figures 5 and 6 the fluid flow velocity streamlines are shown for four and six rotor configurations, respectively.
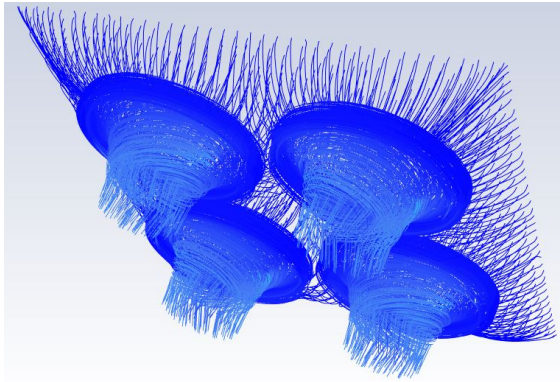
Figure 5. Fluid flow velocity streamlines for four rotors configuration CFD model.
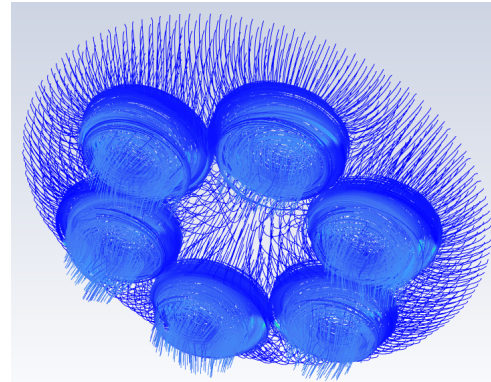

Figure 6. Fluid flow velocity streamlines for six rotors configuration CFD model.

4. Prototype design and field experiments

A six-rotor robot was selected for field work because it had sufficient lifting capacity to work with the sensor mounted on the arm while generating less disturbance than an eight-rotor robot. The robot is equipped with six sets of: BLDC motors, a 30 A ESCs and a 10 inch propellers.
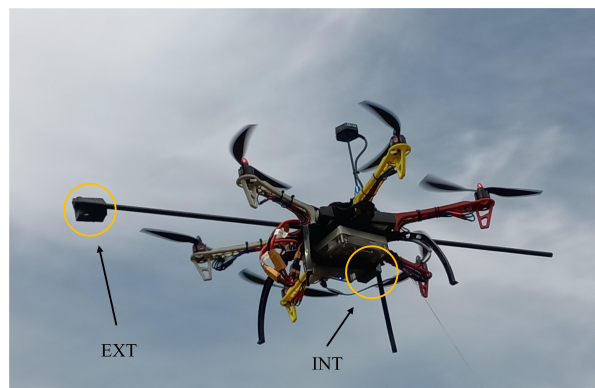

Figure 7. The hexacopter robot in the air.

The maximum lifting capacity of this robot is equal to about 5.16 kg, and it has been equipped with batteries that, according to estimates, should provide about 25 minutes of flight time. The robot was equipped with a symmetric external arm. Its length in relation to the robot's COG was 0.5 m. The first PM sensor was placed on the arm in front of the robot and the second PM sensor (both PMS5003 type) was installed under the robot. Such a solution was chosen because the sensor mass was not large and the direct assembly on the arm did not affect its measurement properties. The Plantower PMS5003 particulate matter sensor has the following (selected) measurement properties: range of measurement 0.3-1.0, 1.0-2.5, 2.5-10.0 μm, resolution of 1 $\frac{\mu m}{m^3}$, single response time < 1 s, and physical size of 50 mm × 38 mm × 21 mm. Figure 7 shows the location of both sensors. The constructed control and measurement system has the ability to collect data from both sensors simultaneously. The following nomenclature will be used from this point on: the internal (INT) sensor is the sensor located directly below the robot and the external (EXT) sensor is the one located on the arm. Therefore, the horizontal

position of the internal sensor is the same as that of the robot. It is located 0.1 m vertically under the propeller axis. Tracking the position of the external sensor was easy because the robot received a constant orientation (forward toward the north) while taking measurements. Therefore, the position of this sensor could be considered as a simple offset. The external sensor is extended 0.5 m horizontally between the axes of the adjacent propellers, while vertically it is 0.05 m below the propeller axis.

The most important aspect of these tests was to check if there is a relationship of some sort between the measured particle concentrations. For this purpose, Pearson's correlations between measured concentrations for five factors measured or determined, such as robot position (X, Y), flight time, flight direction, and distance from pollution sources, were examined. In addition to these, there were still three not measured factors, such as the intensity of the pollution source and the speed and direction of the wind. During the tests, the concentration of particles PM_{10} was analyzed because they covered the vicinity of the particles counted by the sensor.

The results from two flights with and without the source of pollution are shown in Figures 8 and 9 are containing the analysis of the PM_{10} concentration measurements on both sensors, visualized as histograms and scatter plots with the Perason correlation coefficient determined. The PM sensors used have a variable sampling time, so it was necessary to resample incoming data to a uniform frequency of 1Hz.
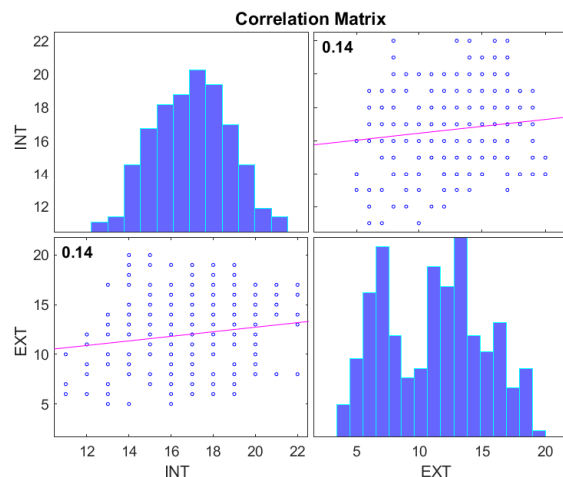

Figure 8. Histogram and correlation of measured PM_{10} without pollution source.
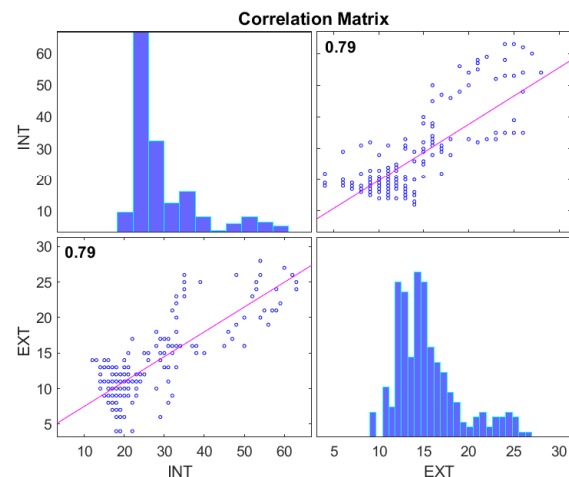

Figure 9. Histogram and correlation of measured PM_{10} with pollution source.

On the basis of the presented data, it can be seen that there is a significant correlation between the measured concentrations in the flight with the source present. The concentration measured on the internal sensor was higher than that measured on the external sensor. For conditions without a source, this correlation does not occur because the concentration of ambient air pollution is fairly constant, so the two averages are compared.

5. Conclusions

In summary, an analysis was performed for the rotor configurations of the robots of the greatest practical importance: quad-, hexa- and octocopter. For those, five cases were modeled and analyzed in this work: two single propellers (10 and 12 inches), counter-rotating pair, four and six rotor configurations. Next, on that basis, it was possible to determine the criterion of a sufficient distance of the PM sensor from the propellers. Then PM measurements were made using the constructed hexacopter robot with the simultaneous use of two sensors: on the extended arm and under the robot. With the data from the field experiments, it is possible to check whether the differences in the measurements can be explained on the basis of the prepared

numerical CFD model. For this purpose, the conditions that occur at the sensors' locations were listed with the mean measured concentrations and presented in table 2. The following symbols were used: R - reference measurement for the flight without S1 and S2 - averages for the flight with the pollution source present. These means of S1 and S2 were determined as averages calculated taking samples below and above the maximum value recorded on the external sensor for the reference measurement, respectively. In the case of an internal sensor, the air speed in

Table 2. Summarized results from the computational model and experiment.

Sensor location	Velocity [m/s] magnitude	Pressure [Pa] static	Pressure [Pa] dynamic	Turbulent [%] intensity	PM_{10} [$\mu g/m^3$] R	PM_{10} [$\mu g/m^3$] S1	PM_{10} [$\mu g/m^3$] S2
INT	0.8723	-0.4729	0.4733	4.46	16.62	21.24	47.17
EXT	0.1768	-0.0198	0.0198	0.89	11.95	11.05	23.37

its surroundings is about five times greater, which may cause a greater accumulation of particles near it. In summary, it should be stated that CFD can explain the existence of differences in measured concentrations at the two analyzed points, providing information on how to design the air pollutant measurement system. The linear dependence between the concentrations measured in Figure 9 was given by equation $PM_{10,INT} = 1.79 PM_{10,EXT} + 1.94$. If such a relationship would be generally correct, as the work carried out shows, then only the sensor located under the robot could be used to calculate the concentrations on the arm without the need for it. However, a general affirmation of the validity of this relationship requires investigation of the impact of changes in pressure and flow speed on the ambient concentration of particles. Plans for such work are planned for the future as well as for comparing the true concentration with the data reported by both sensors. To achieve this goal, it is necessary to perform reference concentration measurements using a robot without rotating propellers. Such measurements can be made by mounting a robot on a long stick in the field or using a dust chamber. Finally, the numerical model also gives the possibility to analyze different configurations of robots. However, the level of disturbance generated by a robot with a larger number of rotors is greater than that with a smaller number of rotors, with the benefit of greater lifting capacity.

Acknowledgments

References
[1] Maciejewska K 2020 *Air Quality, Atmosphere & Health* **13** 659–72
[2] Holder A L *et al.* 2020 *Sensors* **20** ISSN 1424-8220
[3] Cichowicz R and Dobrzański M 2021 *Energies* **14** ISSN 1996-1073
[4] Mayuga G P *et al.* 2018 Airborne particulate matter monitoring using uavs for smart cities and urban areas *TENCON 2018 - 2018 IEEE Region 10 Conference* pp 1398–1402
[5] Cashikar A *et al.* 2019 *Journal of Environmental Engineering* **145** 04019057
[6] Narayana M V *et al.* 2022 *Sensors* **22** ISSN 1424-8220
[7] Rohi G *et al.* 2020 *Heliyon* **6** e03252 ISSN 2405-8440
[8] Koziar Y *et al.* 2019 Quadrotor design for outdoor air quality monitoring *2019 IEEE 39th International Conference on Electronics and Nanotechnology (ELNANO)* pp 736–739
[9] Hedworth H A *et al.* 2021 *Journal of Aerosol Science* **152** 105702 ISSN 0021-8502
[10] Zhang B *et al.* 2018 *Meteorology and Atmospheric Physics* **130** 383–92
[11] Li H *et al.* 2020 *Atmosphere* **11** ISSN 2073-4433
[12] Ansoft Inc. 2020 *Ansys Fluent Theory Guide. Release 2020 R1*
[13] Batchelor G K 1967 *Cambridge Univ. Press. Cambridge, England*
[14] Romik D and Czajka I 2022 *Energies* **15** ISSN 1996-1073
[15] Franzke R *et al.* 2019 *Energies* **12** ISSN 1996-1073